A Final Report to

Honeywell Engines, Systems & Services
Phoenix, AZ

ON

Plasma Actuated Azimuthal Cascade Flow Vectoring: Final Report

BY

Thomas Corke

University of Notre Dame
Institute for Flow Physics and Control
Hessert Laboratory for Aerospace Research
Notre Dame, IN 46556
(574) 631-3261 (Tel)
(574) 631-8355 (Fax)
tcorke@nd.edu

November, 2016

Summary

Experiments were performed with the objective of investigating the use of plasma actuators to replace mechanical variable geometry (VG) inlet guide vanes (IGVs) in Honeywell turbomachines. The experimental setup consisted of an azimuthal array of vanes of two cross-section shapes. One had a circular cross section. For this, different cylinder diameters and array solidities were investigated. The other shape was a full-scale Honeywell IGV geometry. The azimuthal arrays were mounted in a specially designed circular duct that allowed a range of inlet flow Mach numbers from 0.1 to 0.6. The plasma actuators were the new Pulsed-DC approach. This was motivated by the substantially lower voltages used with the Pulsed-DC plasma actuator that provided the capability of locating the actuator on small trailing-edge radii of Honeywell IGVs. Various locations and operation conditions of the Pulsed-DC plasma actuators were examined in order to seek the most effective flow vectoring capability. The flow vector angles were measured using two approaches. One was based on a 5-hole Pitot probe. The second used a standard Pitot probe that was capable of traversing across the wake of one of the vanes. Finally, flow vectoring for a 2-D circular cylinder with both Pulsed-DC and the previous AC plasma approach were compared in a wind tunnel. These experiments indicated that the transient nature of the Pulsed-DC actuator affected its performance for flow separation control, and therefore flow vectoring control. As a result, the choice of the pulsing frequency was found to be important. To be most effective, the pulse frequency needed to be chosen to interact with the separated shear layer instability frequency. This was not the case for the AC actuator which produced a quasi-steady effect on the separated flow.

1 Experimental Approach

The experiments were performed in a specially designed circular test section with a center body that was designed to hold an azimuthal array of IGVs. A CAD drawing of this arrangement is shown in Figure 1. The inside diameter of the outer duct was 9 in. The maximum outside diameter of the center body was 5.8 in. This provided a passage dimension of 1.60 in. All of the components of the test section were made from an Aluminum alloy. The center body was fabricated from six pieces. These were machined to produce an elliptic cross-section profile that transitioned into the constant center body diameter at the axial location that was slightly upstream of the vane array. This is illustrated in Figure 2.

The test section was mounted to an inlet of the Hessert Laboratory Tri-sonic Wind Tunnel. The wind tunnel is driven by two variable R.P.M. vacuum pumps. Test sections are mounted to a central manifold that is connected to the vacuum pumps. The vacuum pressure in the manifold can be set anywhere between 760 to 380 Torr. Air is drawn through the test section from the laboratory space, which is at atmospheric pressure. Based on the maximum flow rate of the vacuum pumps, pressure drop through the test section, and the passage cross-section area, inlet flow Mach numbers of up to 0.7 could be achieved in the experiment. Note that the same facility was used for the linear cascade experiments under the recently completed Honeywell program. Figure 3 shows photographs of the test section mounted to the inlet vacuum pumps manifold.

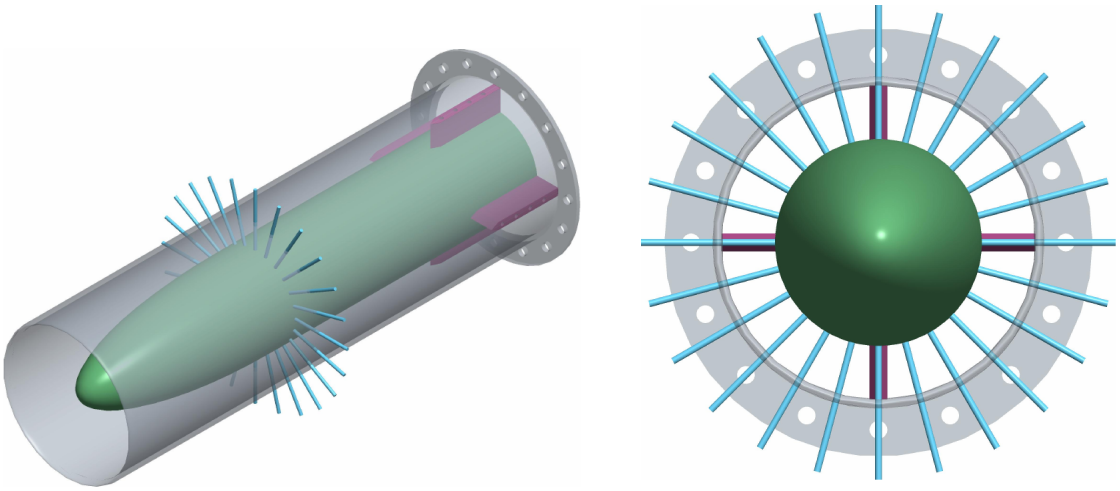

Figure 1: CAD drawing of the circular test section with center body containing an array of 24 circular cylinders.

The circular test section was designed to hold up to 24 IGV elements. Different shaped elements were examined. The first shapes examined were circular cylinders. Two diameter cylinders were investigated. The first had a diameter of 3/16 in. With this diameter the aspect ratio for the cylinder in the passage was 8.5, the maximum area blockage was 2.5%, and the area blockage at the center span of the passage was 1.54%. The second cylinder diameter was 1/2 in. This resulted in an aspect ratio in the passage of 3.2, a maximum area blockage was 17%, and the area blockage at the center span of the passage was 11%. Only an

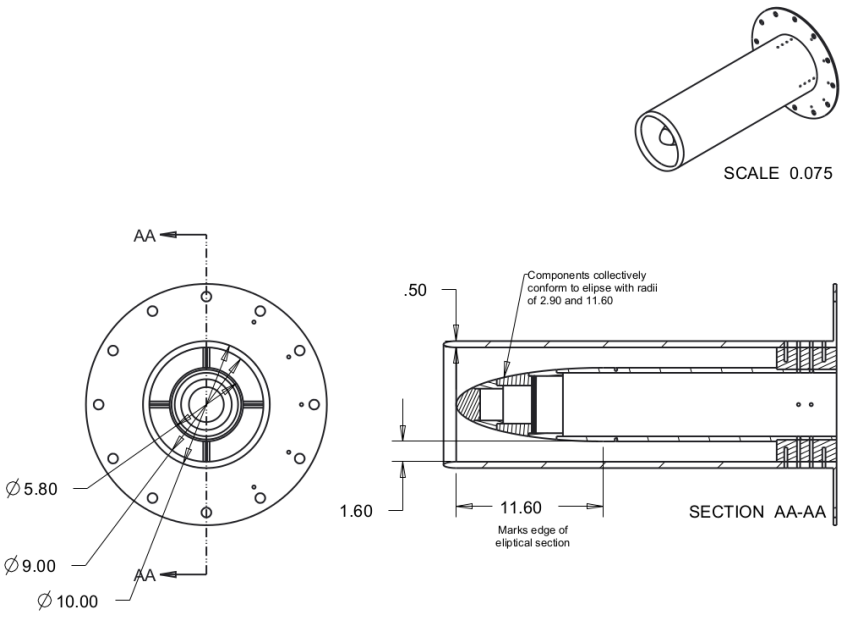

Figure 2: Drawings of the circular test section with center body with sectional view showing the fabrication for the parabolic leading portion that transitioned into the constant diameter body. All dimensions in inches.

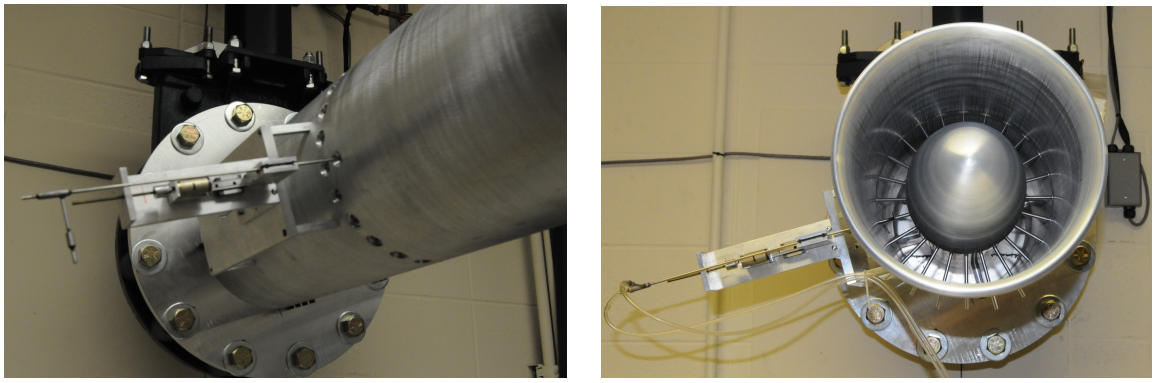

Figure 3: Photographs of the circular test section with center body attached to the vacuum pumps manifold.

array of five 1/2 in. diameter cylinders were used. The purpose of using the larger diameter was to reduce the sensitivity on locating the plasma actuator at the flow separation location, where it should be most effective.

The cylinders were made of non-conductive Lexan. The plasma actuator consisted of a covered electrode that was wrapped around the downstream 180° portion of the cylinder. This electrode was covered by two 2 mil (0.002 in.) thick layers of Kapton film that wrapped completely around the cylinder. The exposed electrode was placed on on top of the Kapton film. One edge of the exposed electrode just overlapped an edge of the covered electrode. The other edge was located approximately 30° upstream of the edge of the covered electrode. This prevented any plasma from forming on the upstream edge of the exposed electrode. Non-conducting end caps were designed and 3-D printed to hold the cylinders in the circular test section. Figure 4 shows the design of these end caps. This allowed them to be rotated to align the plasma actuator with the flow separation location, and to insulate the wiring from the Aluminum duct walls. Figure 5 shows one of the 3/16 in. diameter cylinders mounted in the end caps, and with the plasma actuator operating. Figure 6 shows a photograph of plasma actuators operating on the array of 24, 3/16 in. diameter cylinders. For this photograph, the cylinders had been rotated 90° towards the test section inlet so that the glow from the plasma actuators was visible.

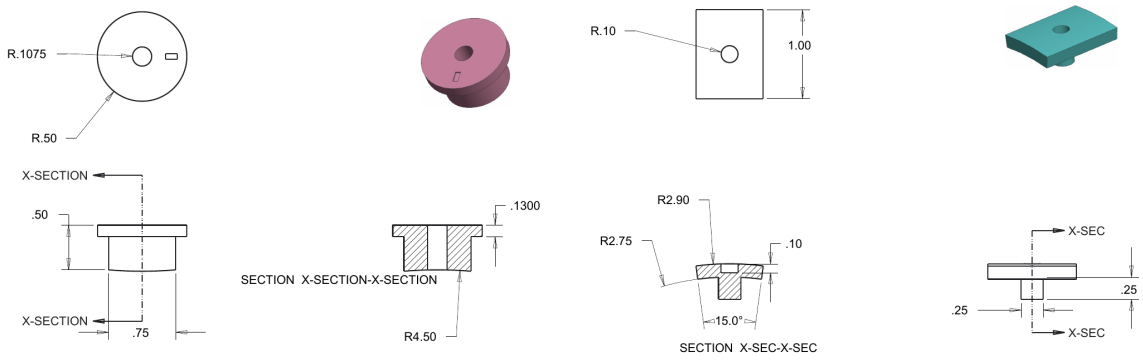

Figure 4: Schematic drawings of the non-conductive end caps for holding the circular cylinders in the circular test section.

The other shape investigated was an IGV vane geometry provided by Honeywell. The schematic drawing is shown in the left part of Figure 7. The chord length of the vanes was 1.497 in. The vanes were designed to be rotated about the quarter-chord location. To accomplish this, the end towards the center body had a circular protrusion that fit into the opening of the end cap that was designed for the 3/16 in. diameter cylinder. The vane end towards the outer duct had a recessed slot. The slot accepted a circular plug that fit into the opening used for the outer duct end caps used to hold the cylinders. The end cap holding the vane allowed the vanes to be rotated to different angles of attack. The design of this end cap is shown in the right part of Figure 7.

The IGV vanes were 3-D printed. Figure 8 shows photographs of a vane alone and with the end cap used in rotating the vanes in the passage. Only five IGV vanes were tested. These were arranged in a group as shown in the schematic in Figure 9.

The plasma actuators were located on the trailing-edge radius of the IGV vanes. The

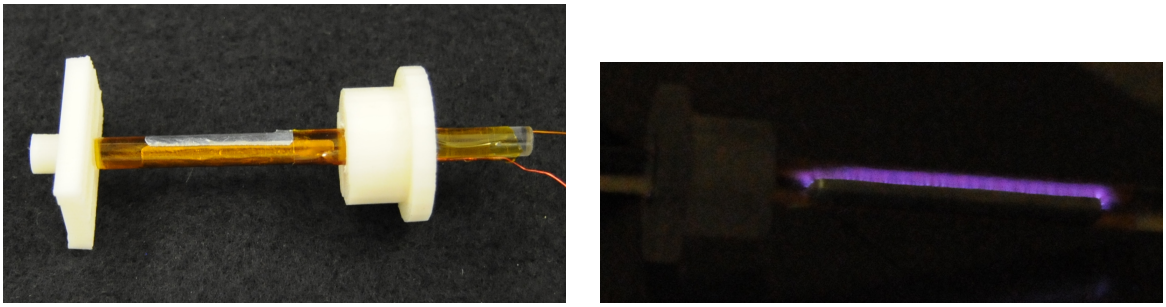

Figure 5: Photograph of 3/16 in. diameter cylinder with plasma actuator mounted in non-conductive end caps (left) and while operating in a darkened lab (right).

Figure 6: Photograph of operating plasma actuators on the array of 24 3/16 in. diameter cylinders in the circular test section. Note that the cylinders had been rotated 90° towards the test section inlet for the glow to be more visible.

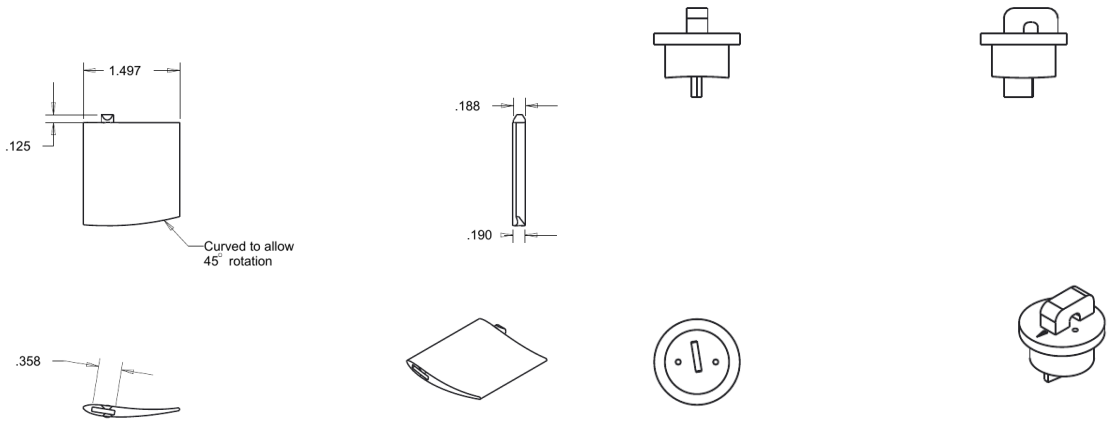

Figure 7: Schematic drawings of the IGV vanes and end cap used to rotate the vane about the quarter-chord location.

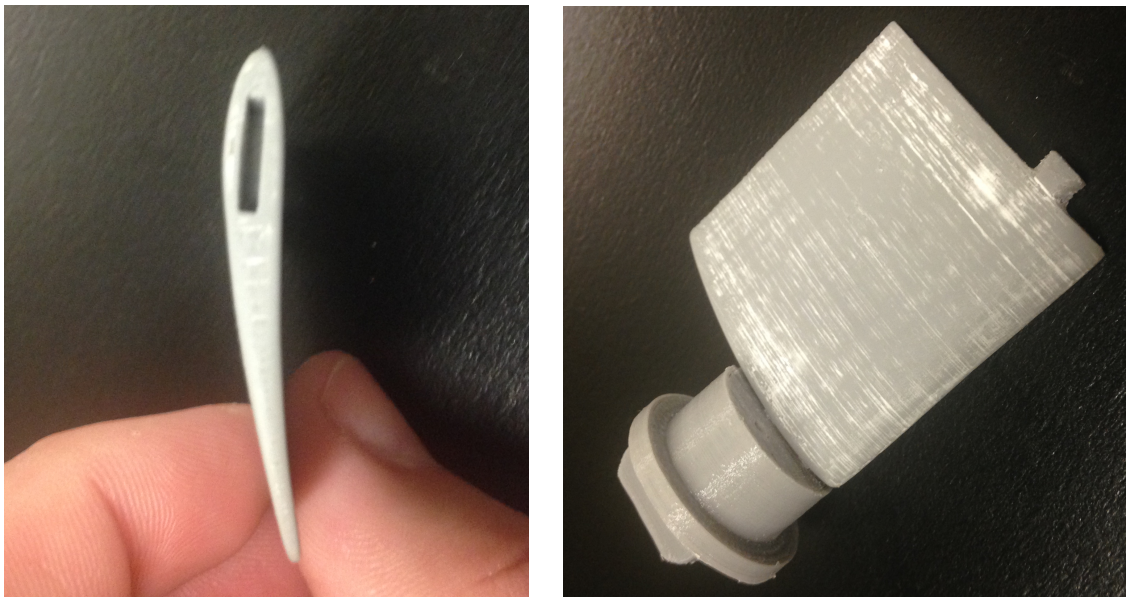

Figure 8: Photographs of the 3-D printed IGV vanes and end cap used to rotate the vane about the quarter-chord location.

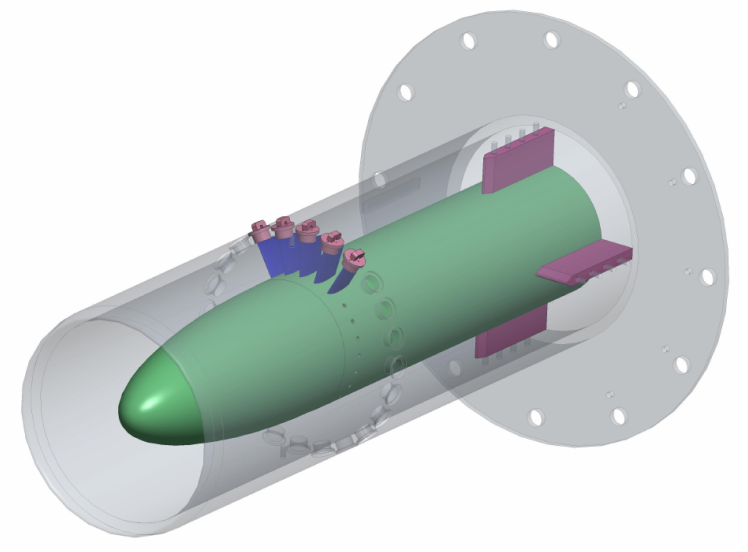

Figure 9: Schematic showing the arrangement of five IGV vanes investigated in the experiment.

construction was similar to that of the circular cylinders. The covered electrode was located on the pressure-side of the vane, covering half of the pressure-side trailing-edge radius. The exposed electrode was then covered by two 2 mil thick layers of Kapton film. The exposed electrode was then placed on the suction side of the vane. It extended to the suction-side half of the trailing-edge radius where it aligned with the downstream edge of the covered electrode. A photograph of the plasma actuator on one of the IGV vanes is shown in the left part of Figure 10. The white power leads shown in the photograph were later changed into the thin power leads that were used with the circular cylinders. The photograph in the right part of Figure 10 shows the plasma that formed at the trailing edge with this actuator design.

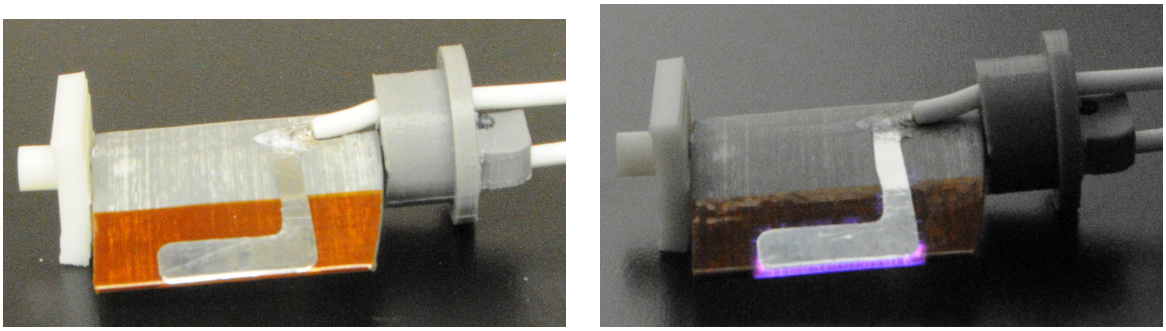

Figure 10: Photographs of the plasma actuator on an IGV vane (left) and while operating (right).

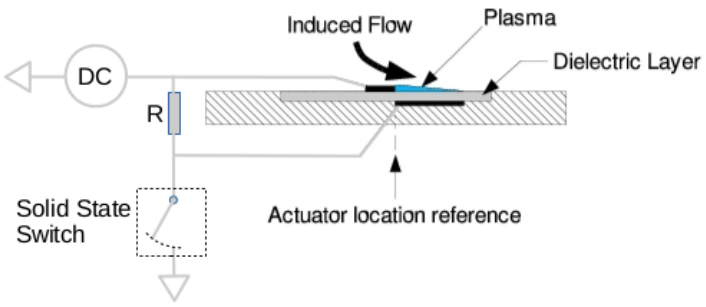

Figure 11: Schematic illustration of the pulsed-DC DBD plasma actuator.

1.1 Pulsed-DC Plasma Actuator

The new approach for operating the plasma actuator is "pulsed-DC". This is designed to be a hybrid approach that embodies the best aspects of AC and DC plasma actuators. The plasma actuator arrangement is identical to most typical AC-DBD designs, with staggered electrodes that are separated by a dielectric insulator. However instead of an AC voltage input to drive the actuator, the pulsed-DC utilizes a DC voltage source. As shown in the schematic for the pulsed-DC plasma actuator in Figure 11, the DC source is supplied to both electrodes. A resistor, R, limits the current to the lower electrode, which is also connected to a fast-acting solid-state switch that when closed, shorts the voltage to the lower electrode to the power supply ground. A periodic trigger signal consisting of a TTL pulse is supplied to activate the solid-state switch.

Figure 12 compares the reaction thrust, proportional to the plasma body force, for the same plasma actuator powered either by the older AC approach or the new pulsed-DC approach. The dielectric layer consisted of two 2 mil. layers of Kapton film. The spanwise length of the actuator was 2.5 in. There are two notable features of the comparison. The first is that with the AC operation, the thrust increase with input voltage displays the characteristic power law relation namely, $T \sim V^{3.5}$, whereas the thrust varies linearly with the pulsed-DC voltage. The second and most striking feature is that the thrust generated by the pulsed-DC actuator is significantly more than that of the AC actuator.

The significantly larger actuator body force at the relatively low voltages allows much thinner dielectric layers to be used. This lended itself to applying the plasma actuator on the small trailing edge radius of the Honeywell IGV that was shown in Figure 8. This was not possible with the AC driven plasma actuator which required significantly thicker dielectric layers that could withstand the necessary higher operating voltages.

We suspected that the short duration of the DC pulse in the Pulsed-DC plasma actuator produced a fundamentally different velocity field compared to that of the AC plasma actuator velocity. Traditionally with the AC plasma actuator, the velocity field that was generated was measured with a glass total-pressure Pitot probe. The glass was necessary to prevent ionization occurring on the probe. An example of the time-averaged velocity profile for an AC plasma actuator, from Post 2004 Ph.D. thesis is shown in the left part of Figure 13. When a similar approach was used to measure the velocity field generated by the Pulsed-DC plasma actuator, the velocity profile, shown in the right part of Figure 13, indicates an order of magnitude lower maximum velocity that is inconsistent with the body force

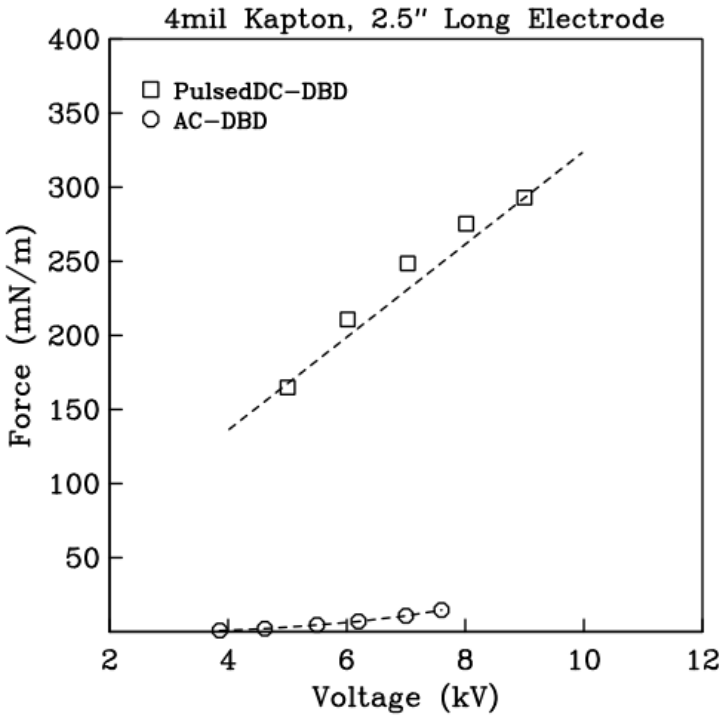

Figure 12: Comparison between the induced thrust for the same plasma actuator operating by either AC and pulsed-DC plasma input.

(thrust) measurements. The issue is that the low frequency response of the Pitot probe system was not capable of measuring the short transient velocity peak that we expected was being produced by the short-duration DC pulse. This was not an issue for the AC plasma actuator which produced a quasi-steady velocity field.

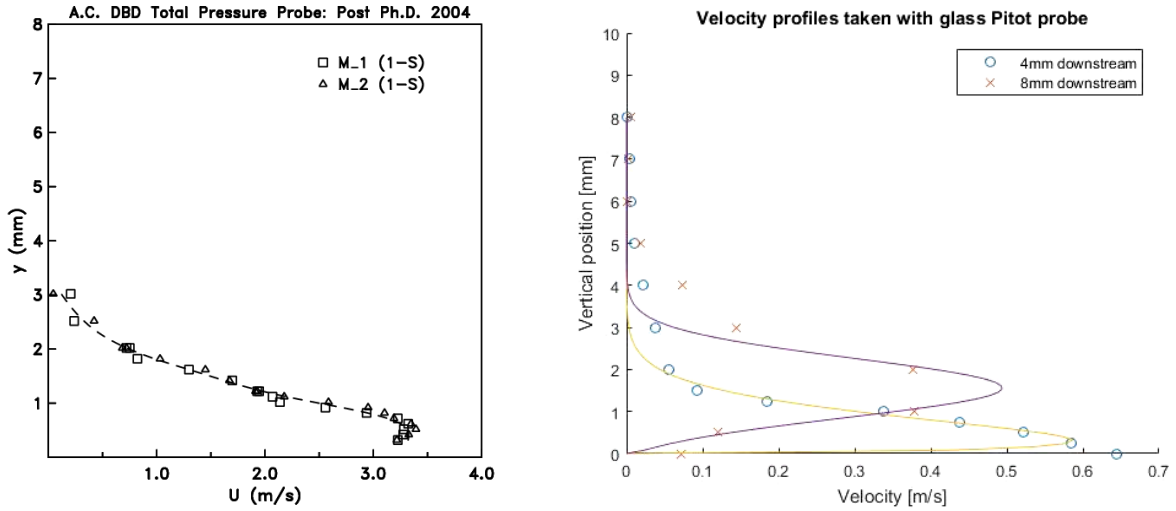

Figure 13: Mean velocity profiles obtained using a glass Pitot probe for an AC plasma actuator (left, from Post 2004 Ph.D.) and from a Pulsed-DC plasma actuator (right).

Therefore in a separate investigation, a hot-wire anemometer system was built that could perform fast time-response velocity measurements close to the plasma actuator. In order to survive in the charged air environment near the actuator, the hot-wire anemometer electronics was designed with a floating ground. The anemometer output was coupled to gain and frequency compensation circuits through a optical coupler consisting of a infrared light source and photo multiplier. This isolated the floating elements from the instrument ground elements. With this approach, the hot-wire was capable of operating even while sustaining plasma discharges as was visibly evident in the photograph in the left part of Figure 14. The right part of Figure 14 shows velocity time series from the Pulsed-DC actuator that was measured with the hot-wire. This indicates a transient short-time peak in the velocity produced by the actuator that quickly dissipates.

Similar velocity time series were acquired at different wall-normal positions above dielectric layer surface. The time evolution of the peak velocities as a function of the wall-normal position is shown in Figure 15. This was measured 4 mm from the edge of the exposed electrode. This is presented as a 3-D plot that shows the wall-normal peak-velocity profile versus time. Time equal to zero corresponds to the start of the DC pulse. The experiment was performed in still air so that prior to the DC pulse, the velocity is zero. The bracket indicates the time duration of the DC pulse. The air velocity builds up from that point in time and reaches a maximum at the end of the DC pulse. The maximum velocity is approximately 6 m/s, which is 20-times that measured with the glass Pitot probe. The wall normal distribution indicates that the peak velocity is approximately 2 mm above the surface, which is considerably higher than that of the AC actuator. The other aspect of these measurements is the rapid decay of the velocity following the DC pulse. Thus the Pulsed-DC

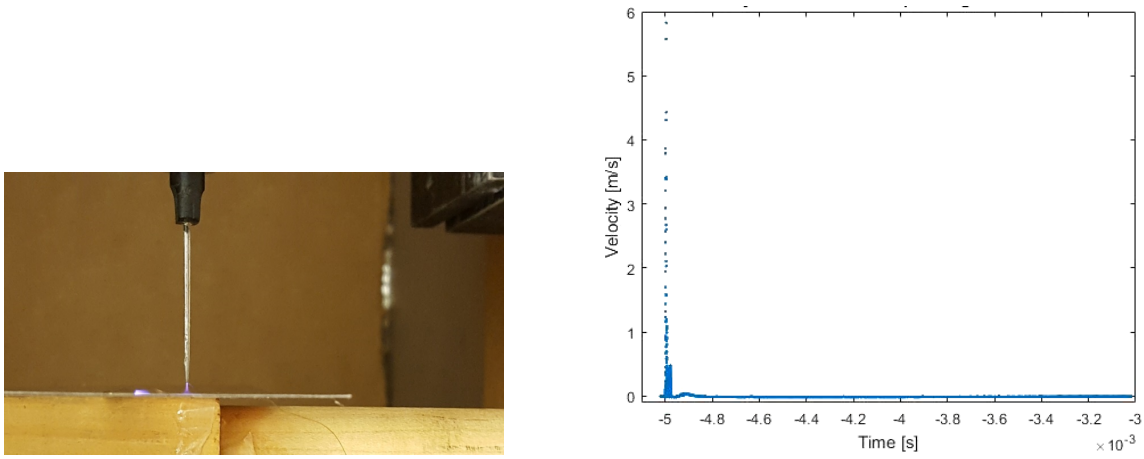

Figure 14: Photograph of the hot-wire during velocity measurements near the Pulsed-DC plasma actuator (left) and sample velocity time series measured by the hot-wire (right).

actuator induced velocity field is highly transient. This has implications on its use for flow control that were not anticipated a priori.

A series of experiments were performed to contrast the flow separation control between the AC and Pulsed-DC actuators. This involved flow particle visualization around a circular cylinder. The cylinder diameter was 1.32 in. The cylinders were 24 in. in length. This larger cylinder was used to be able to place two plasma actuators at 90° and 125° locations from the stagnation line. The plasma actuators extended along the full length of the cylinders. The experiments were performed in a wind tunnel. Flow visualization particles were introduced upstream of the cylinders. The flow pattern was recorded with a camera with a slow (10 s.) shutter speed to obtain time-averaged images. The particle visualization requires low free-stream speeds that ranged from 2 m/s to 3.1 m/s.

Figure 16 shows flow visualization images for a single Pulsed-DC plasma actuator at the 90° location at a free-stream speed of 2 m/s. The three images correspond to the baseline condition with the actuator off, and with the Pulsed-DC actuator operating at pulsing frequencies of 500 Hz and 100 Hz. The single actuator at the 90° location is expected to reduce the extent of the wake closer to the actuator, and to vector the flow towards the opposite side of the cylinder. The dashed curves overlying the images provides a guide to these two flowfield characteristics. Based on these two metrics, we judge the 100 Hz pulsing frequency to be more effective. We do not know if it is optimum in this case. Now any dependence on frequency is a dynamic effect, and it is well known that unsteady forcing near the separated shear layer Kelvin-Helmholtz instability frequency is an effective method of flow separation control. This would account for the dependence on the pulsing frequency. More importantly, it indicates that the selection of the pulse frequency is important in the effectiveness of the Pulsed-DC actuator. This is not the case with the AC actuator, where the Pitot probe measurements indicate that the induced velocity field is quasi-steady. This actually is a large advantage in the flow simulations that include the effect of the AC plasma actuator.

The effect of using a pair of Pulsed-DC actuators located at 90° and 125° is shown in Figure 17 for a higher free-stream speed of 3.1 m/s. The Pulsed-DC actuator in this case is

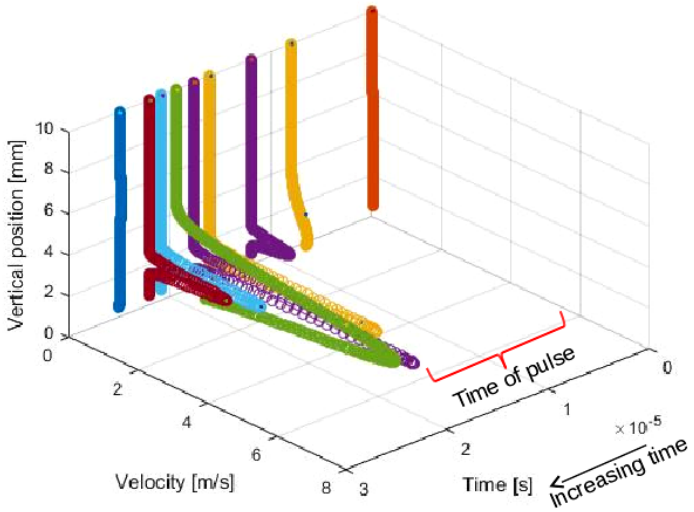

Figure 15: Time-resolved wall-normal peak-velocity profiles of the induced flow measured 4 mm from the exposed electrode of the Pulsed-DC plasma actuator.

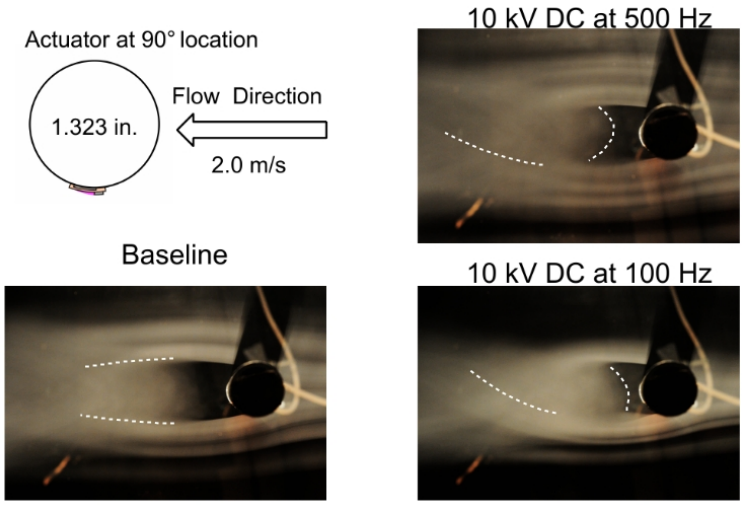

Figure 16: Flow visualization images for a single Pulsed-DC plasma actuator at the 90° location at a free-stream speed of 2 m/s that compares the effect of the Pulsed-DC frequency.

operated at 100 Hz. Contrasting the baseline visualization image with that with the actuator operating, the flow vectoring effect is clearly evident. Comparing this case with that with a single actuator that was shown in Figure 16 indicates only a marginal difference that does not necessarily merit using a second actuator. For reference, flow visualization the same conditions with the actuator operated with an AC voltage is shown in Figure 18. The AC plasma actuator in this case is operated at a slightly higher voltage of 12 kVp-p. The power levels to the AC actuator were however two orders of magnitude larger than that of the Pulsed-DC actuator. The effect of the AC actuator on the flow field is observed to be very similar to that of the Pulsed-DC actuator. However the effect of the AC actuator on the flow field is a *steady effect* whereas that of the Pulsed-DC is an unsteady effect. This makes the use of the Pulsed-DC actuator somewhat more complex in that the choice of the pulsing frequency must be made with some a priori knowledge of the flowfield.

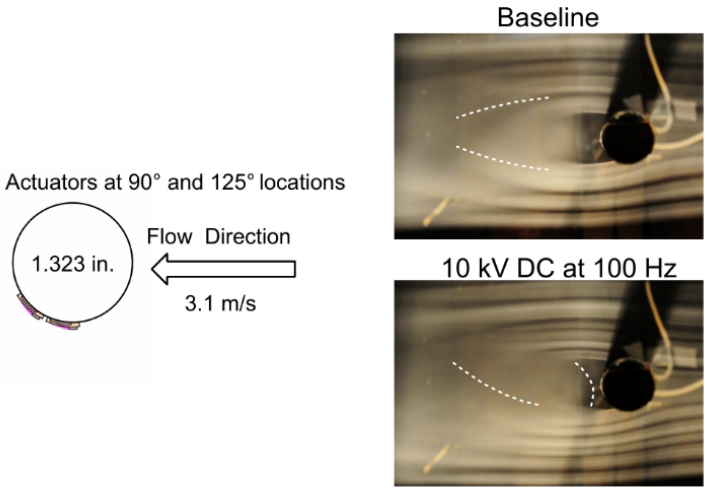

Figure 17: Flow visualization images for a pair of Pulsed-DC plasma actuator at the 90° and 125° locations at a free-stream speed of 3.1 m/s.

Additional evidence of the flow vectoring produced by the Pulsed-DC actuator was obtained through tufts placed on the cylinder surface. This involved a single actuator at the 90° location on a 1/2 in. diameter cylinder. The cylinder was placed in the same wind tunnel test section that was used for the particle flow visualization experiments. An azimuthal array of 1/2 in. diameter cylinders was also tested in the circular test section.

A string tuft was placed at the half-span location of the plasma actuator. The tuft was attached to the front stagnation point so that with the flow it wrapped around the leading portion of the cylinder. Figure 19 shows a sequence of images for different pulsed-DC voltages from 0 to 9 kV. The DC pulsing frequency for the plasma actuator was 500 Hz, which was the same used for the azimuthal array experiments in the circular test section. The flow is from right-to-left. The freestream Mach number was 0.1, which is close to the maximum in the wind tunnel.

When the plasma actuator was off, the tuft was relatively steady and extended in the flow direction. With the plasma actuator at 5 kV, the mean (time-averaged) tuft angle was deflected towards the wake centerline. This is an indication that the flow separation location had been moved aft of the baseline condition which is expected to be 90° from

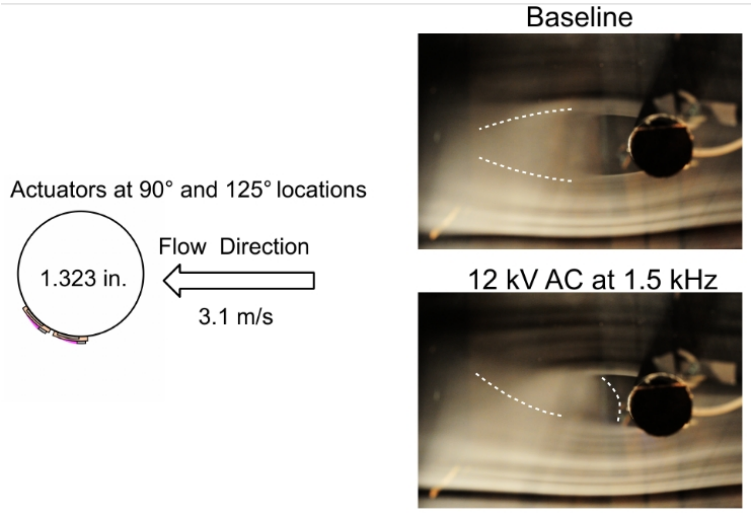

Figure 18: Flow visualization images for a pair of AC plasma actuator at the 90° and 125° locations at a free-stream speed of 3.1 m/s.

the stagnation line. The tuft was noticeably more unsteady compared to the actuator off condition, although the average flow vector angle was approximately 15°.

With the plasma actuator at 7 kV, the mean (time-averaged) tuft angle appeared to increase. Our estimate is a flow vector angle of approximately 20°. The average flow vector angle increased further with the voltage at 9 kV. Our estimate is that the average vector angle was from $30 - 40°$. However the unsteadiness in the tuft appears to increase as the flow turning angle increased.

Overall these results appear to be consistent with the particle flow visualization previously presented, and very similar to the tuft visualization previously performed in a linear cascade. The experiments then proceeded to investigate the azimuthal array of cylinders.

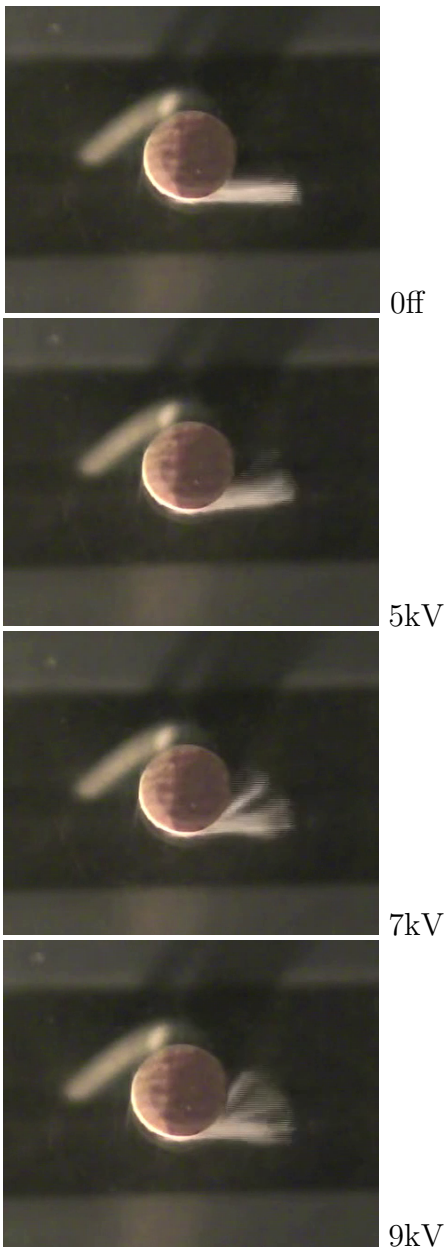

Figure 19: Tuft visualization of the flow directly downstream of a pulsed-DC plasma actuator designed to attach the flow for flow vectoring.

2 Experimental Approach

The flow vector angles were primarily measured using a 5-hole Pitot probe. The same probe was used in measuring the flow turning angles in previous linear cascade measurements. It will be calibrated to measure flow vector angles of ±40°. The 5-hole probe was mounted on a traversing mechanism that was located outside of the duct. This can be viewed in the photographs that were shown in Figure 3. The probe body entered through an azimuthal slot in the outer duct wall. The slot was sealed to prevent air leakage into the duct. Figure 20 shows a schematic with the 5-hole Pitot probe location. As indicated by the right part of the figure, the measurements were taken on the centerline of the top-center IGV (cylinder) in the array. The dimension of the 5-hole probe relative to a 3/15 in. diameter cylinder in the array is also indicated. The downstream measurements location of 4.03 in. corresponded to approximately 21.5 diameters of the 3/15 in. diameter cylinders.

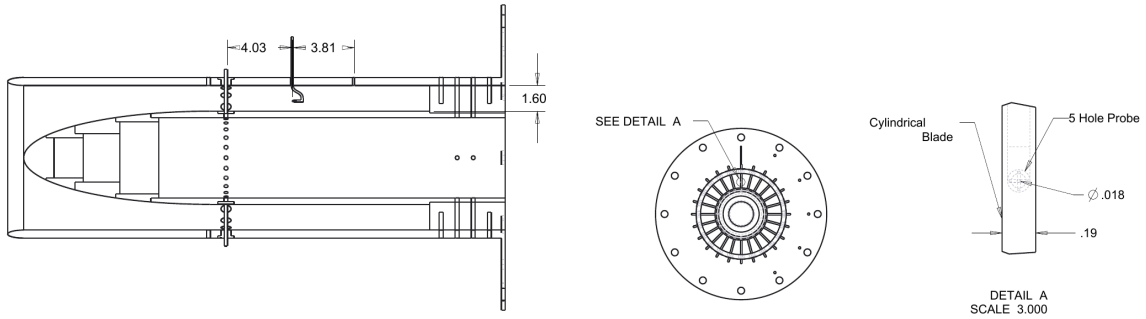

Figure 20: Schematics of the circular test section with a center body that shows the location of the 5-hole Pitot probe.

A later variation of the experimental setup allowed the Pitot probe to be moved upstream and to be pivoted so that velocity profiles across the wake of the top-center IGV (cylinder and vane) could be measured. In this case the 5-hole probe was replaced with a conventional Pitot-static probe.

3 Results

3.1 3/16 in. Cylinder Azimuthal Array

The following results correspond to the 3/16 in. diameter cylinder azimuthal array. The measurements were obtained using the 5-hole Pitot probe from which the mean velocity and pitch and yaw angles could be derived. The results correspond to three free-stream speeds corresponding to inlet Mach numbers of 0.10, 0.15 and 0.20. Higher Mach numbers were not investigated because the flow vectoring effect diminished with increasing Mach number. The pulsed plasma actuator was operated at a DC voltage of 7 kV. Based on the tuft flow visualization experiments, which were produced afterwards, this voltage should have produced flow turning angles on the order of 20° at Mach 0.1. The quantities that were documented by the 5-hole Pitot probe were the dynamic and static pressures from which

the streamwise, U, wall-normal, V, and wall-parallel, W, velocity components were derived. These were then used to calculate the mean flow vector $U-V$ pitch and $U-W$ yaw angles.

In order to use the 5-hole probe for these measurements, it was important that the probe was not influenced by the wake of the cylinder. Recall that the Pitot probe was located on the centerline of the top-center cylinder. This was verified from the streamwise, U, velocity profiles that documented that the probes were always measuring the free-stream velocity appropriate to the Mach number. As an example, Figure 21 shows the U-component profiles for Mach 0.1 and 0.2 cases. Note the convention on these and other similar plots, the ordinate is the position in the channel with 0 corresponding to the surface of the center body, and 1 corresponding to the surface of the outer duct. The line convention has the baseline (plasma actuator off) quantity marked by the circle symbol, and the quantity with the plasma actuator operating marked by the triangle symbol. The results documented virtually no change between the actuator being off or on in the U velocity component, which was expected.

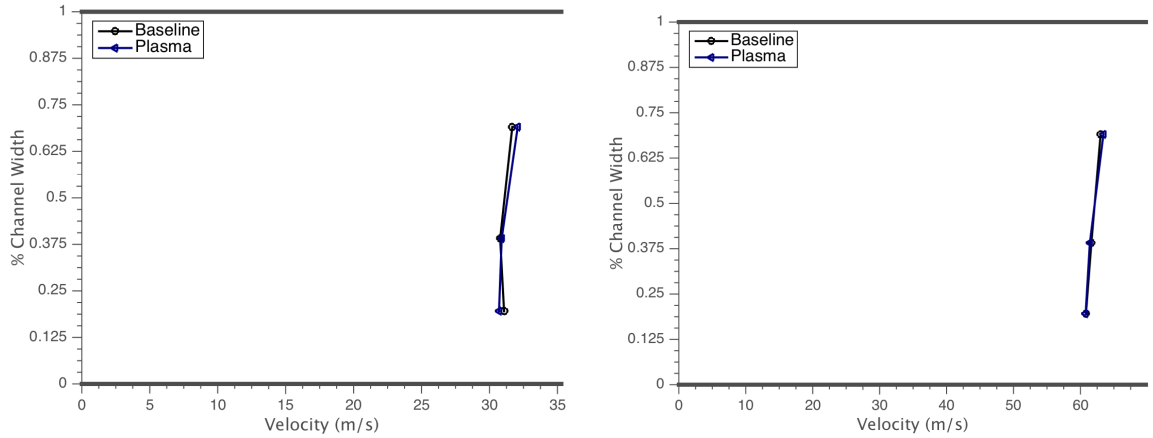

Figure 21: U-component profiles for Mach 0.1 (left) and 0.2 (right) cases measured 21.5 diameters downstream of the 3/16 in. diameter cylinder azimuthal array.

The change in the wall-parallel velocity component, W, through the passage for the Mach 0.1 and 0.2 cases is shown in Figure 22. In both cases, the baseline W velocity exhibits a variation across the passage with a maximum occurring at approximately 38% of the passage width from the center body. This variation is thought to be due to the radially-variable solidity of the IGV cylinder array. The radial distribution changes somewhat with the plasma actuator operating. In the Mach 0.1 case for example, if the maximum change in the W component is taken, and based on the free-stream velocity, the resultant $U-W$ yaw angle is approximately 2°.

The $U-W$ yaw angles across the passage that were directly measured with the 5-hole Pitot probe are presented in Figure 23. The radial variation across the passage reflects the radial variation in the W velocity component shown in the previous figure. The effect of the plasma actuator varies with the radial location. For the Mach 0.1 case, the largest change with the actuator operating occurs at 38% of the passage width. At this location the yaw angle is approximately 1°. In the Mach 0.2 case, the maximum yaw angle occurred at a further outboard radial location of approximately 70% of the passage width. There, the yaw angle was approximately 0.5°.

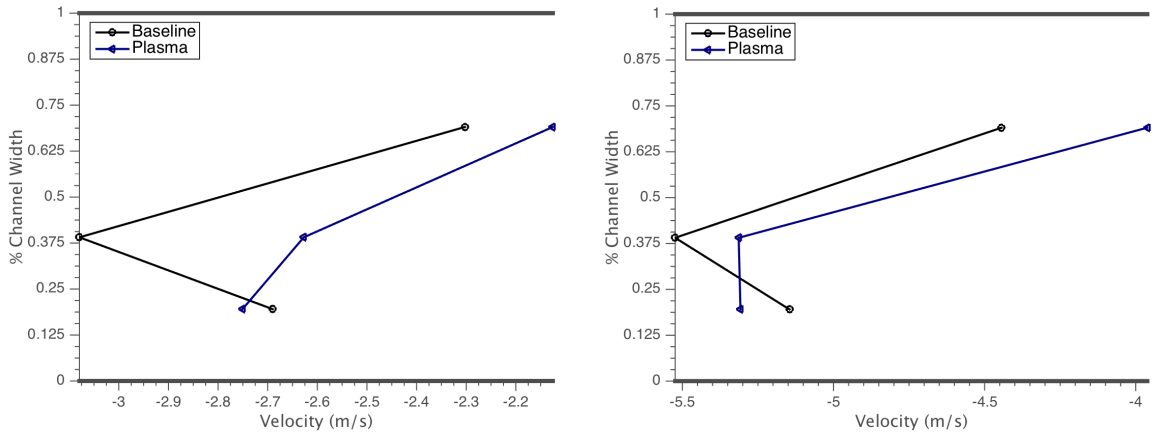

Figure 22: W-component profiles for Mach 0.1 (left) and 0.2 (right) cases measured 21.5 diameters downstream of the 3/16 in. diameter cylinder azimuthal array.

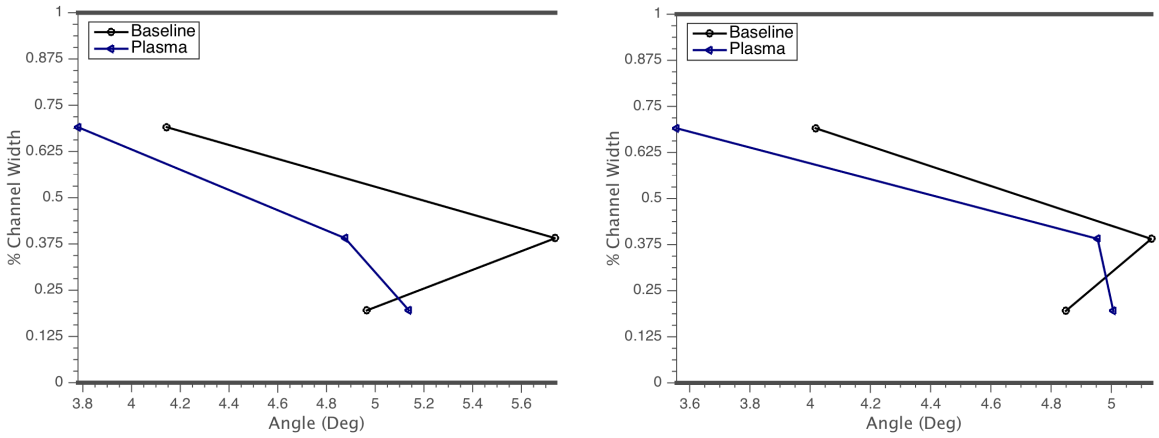

Figure 23: Velocity yaw angle profiles for Mach 0.1 (left) and 0.2(right) cases measured 21.5 diameters downstream of the 3/16 in. diameter cylinder azimuthal array.

3.2 1/2 in. Cylinder Azimuthal Array

The underwhelming results with the azimuthal array of 3/16 in. diameter cylinders prompted us to investigate larger 1/2 in. diameter cylinders in the array. This change was primarily motivated by the sensitivity of the flow vectoring control on locating the plasma actuator (exposed electrode) as close as possible to the flow separation location on the cylinder. This location is nominally 90° from the stagnation line for a laminar boundary layer over the cylinder. It moves aft by a few degrees if the boundary layer is turbulent. This location can also be affected by the blockage produced by neighbor cylinders in the array. Attempts were made to systematically adjust (rotate) the individual 3/16 in diameter cylinders to try to maximize the change in the yaw angle with the plasma actuator operating. Ultimately this was difficult to achieve with the smaller diameter cylinders. Therefore we opted to increase the cylinder diameter to 1/2 in. The selection was supported by the tuft visualization experiments previously discussed in Section1.1 that indicated the effectiveness of the Pulsed-DC plasma actuator in attaching the flow and vectoring the wake.

The setup with the 1/2 in. diameter cylinders consisted of having five cylinders in the azimuthal array. These were located so that the middle cylinder in the array was at the top-center location, placing it on the axial centerline of the 5-hole Pitot probe. All five cylinders had plasma actuators that were designed identical to that on the 3/16 in. diameter cylinders. Only Mach 0.1 was investigated. The DC voltage to the actuator was 7kV, which in the tuft visualization was found to produce a flow turning angle of 15-20 degrees.

The measurements were performed at two downstream locations of 5 and 6 diameters. The results are shown in Figures 24 and 26. With these, the streamwise, U, velocity distributions are shown in the left plot, and the $U - W$ yaw angle distributions are shown in the right plot. The baseline condition is shown by the circle symbols, and the condition with the plasma actuator operating is shown by the triangle symbols. Again the ordinate indicates the percent location across the passage, with 0 being the surface of the center body and 1 being the surface of the outer duct.

For the streamwise, U, velocity measurements taken 5 diameters downstream of the cylinder array and shown in the left plot in Figure 24, the higher blockage of the array in the lower part near the center body gave erroneous values for the baseline condition and therefore were not included in the plot. This was not a problem with the actuator operating where the wake vectoring directed higher-speed flow towards the cylinder centerline location of the Pitot probe. In both cases, the radial distribution of the streamwise velocity varied with the linear radial change in the array solidity. The effect of the plasma actuator was to vector the wake so that the centerline velocity increased. This process is depicted in Figure 25. The measurements indicated in this process the streamwise velocity increased approximately 10 m/s or approximately 30% of the free-stream velocity value. The results show that this effect was uniform along the long axis of the cylinder IGV.

The $U - W$ yaw angle results are shown in the right plot in Figure 24. There again measurements for the baseline condition were only possible for outboard radial locations. Considering the most inboard radial location at approximately 40% of the passage from the center body, the change in the yaw angle is approximately 14°, which is consistent with the tuft visualization.

Moving to a further downstream location of 6 diameters allowed valid baseline velocity measurements closer to the center body. This is documented in Figure 26. For the streamwise velocity component shown in the left plot in the figure, the magnitude again increased approximately linearly with increasing radial position. The effect of the plasma actuator

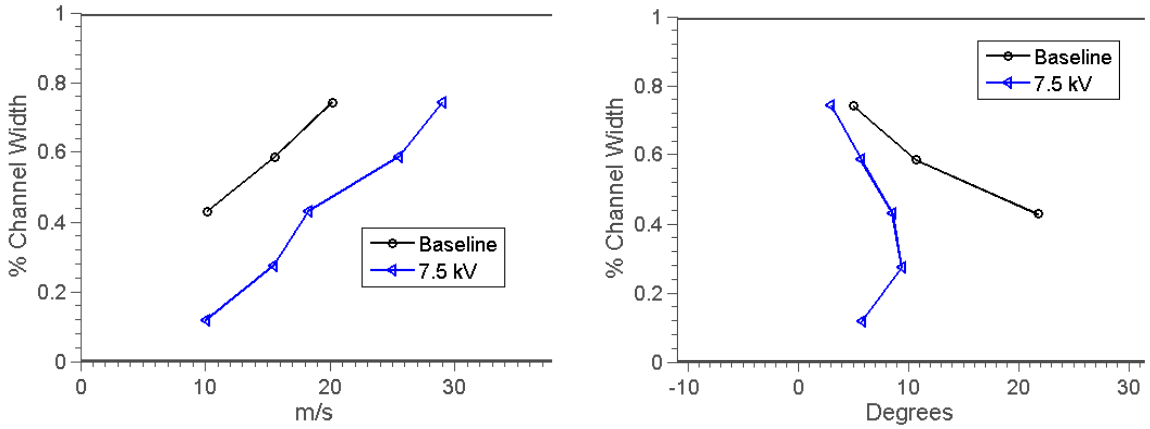

Figure 24: Streamwise velocity (left) and yaw angle (right) profiles for the 1/2 in. diameter cylinder azimuthal array measured 5 diameters downstream at Mach 0.1.

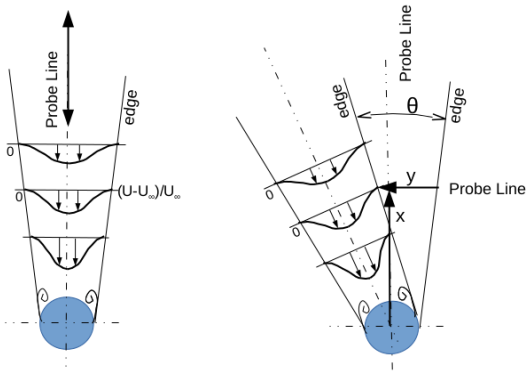

Figure 25: Streamwise velocity (left) and yaw angle (right) profiles for the 1/2 in. diameter cylinder azimuthal array measured 5 diameters downstream at Mach 0.1.

further confirmed the 10 m/s increase in the velocity at the centerline of the top-most cylinder that was previously documented one diameter further upstream. The corresponding radial distributions of the $U - W$ yaw angle is shown in the right plot of the figure. This shows a similar result to that measured at the 5 diameter location, in terms of the shape of the radial distribution and the effect of the plasma actuator. Since these measurements were taken separately and at different times, it indicates very good repeatability of the results.

The results with the 1/2 in. cylinder were encouraging. No attempt was made to investigate higher Mach numbers for this configuration. To do that we would have needed to assemble the full array of 24 cylinders, which was deemed to be too time consuming at the late stage of the investigation. There was also some concern about the blockage the full array might produce, particularly near the center body. Therefore the final set of measurements focused on the airfoil blade IGV.

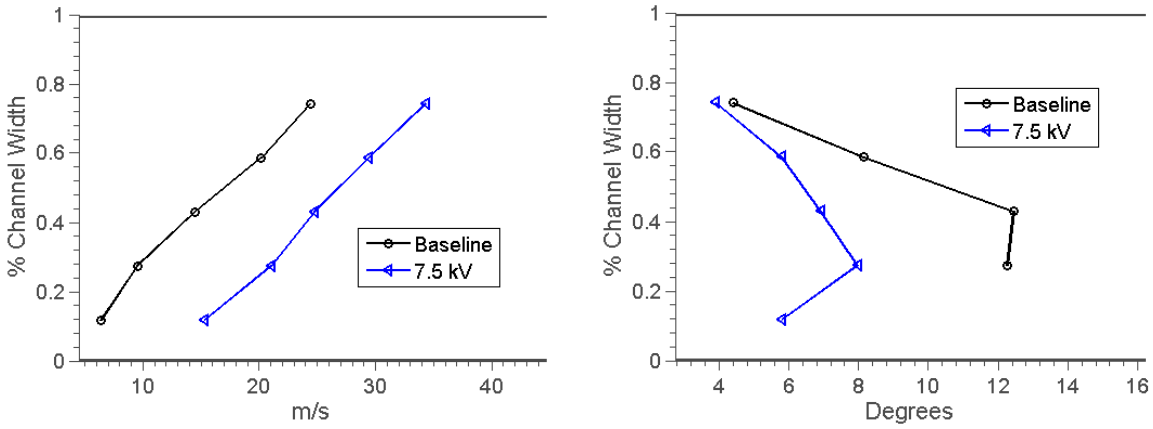

Figure 26: Streamwise velocity (left) and yaw angle (right) profiles for the 1/2 in. diameter cylinder azimuthal array measured 6 diameters downstream at Mach 0.1.

3.3 Airfoil IGV Azimuthal Array

As with the 1/2 in. cylinders, the airfoil IGV setup consisted of having five vanes in the azimuthal array as was depicted in Figure 9. These were located so that the middle vane in the array was at the top-center location. All five vanes had plasma actuators that were designed identical to that on the 3/16 in. diameter cylinders.

Two different plasma actuator configurations were investigated. The one shown in the drawing in Figure 27 placed the plasma actuator on the suction side of the trailing edge. It was oriented so that the body force vector was directed in the mean flow direction. This is the configuration that was shown in Figure 10. The objective of this was to produce an effect like that of a plane trailing edge flap with a positive flap deflection that would vector the flow towards the suction side of the vane.

A second plasma actuator configuration that was examined is shown in Figure 28. In this case, the plasma actuator was placed on the pressure side of the vane near the trailing edge. The actuator was oriented so that the body force vector was directed in the upstream direction. The purpose was to cause the boundary layer on the vane to separate near the

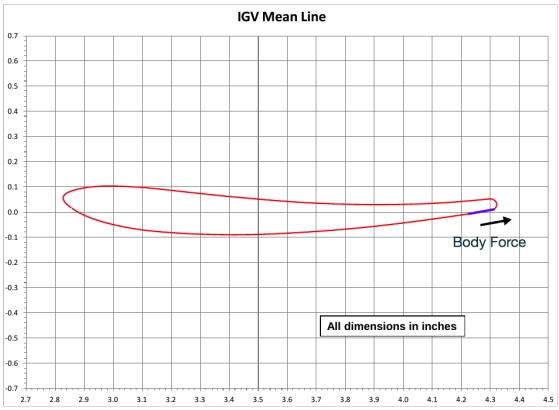

Figure 27: Fabricated IGV vane section shape (shown to scale) with plasma actuator located on the suction side of the trailing edge.

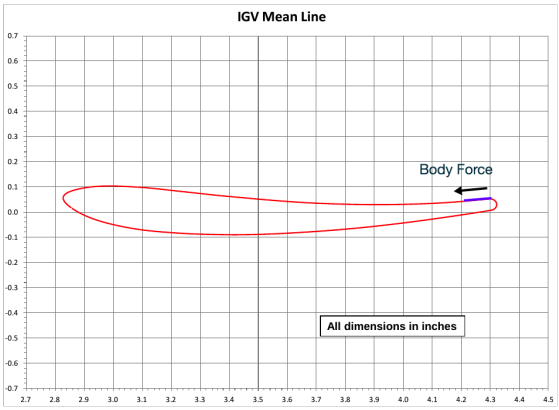

Figure 28: Fabricated IGV vane section shape (shown to scale) with plasma actuator located on the pressure side of the trailing edge.

trailing edge producing an effect that is similar to a Gurney flap. A Gurney flap on the pressure side will produce an effect that is similar to that of a plane flap with a positive angle of attack and therefore vector the flow towards the suction side of the vane. This effect is illustrated in Figure 29.

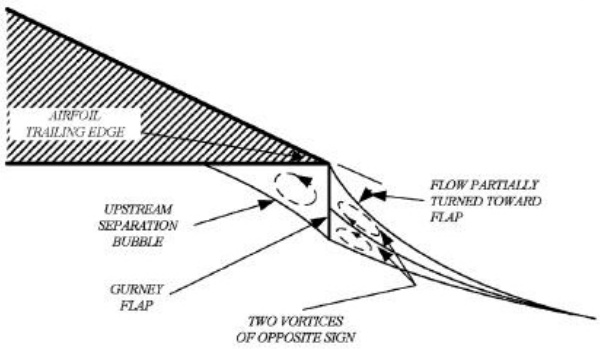

Figure 29: Illustration of flow field produced by Gurney-flap-induced trailing-edge flow separation.

3.3.1 Suction-side Actuator

All of the experiments involved a *single* actuated vane at a free-stream Mach number of 0.1, and with the pulsed-DC voltage amplitude of 9 kV. Mean velocity profiles were measured $0.42c$ downstream of the trailing edge of the vane at a radial location corresponding to 39% of the distance from the center body. Figures 30 to 33 correspond to the cases with the plasma actuator located on the suction side of the vane as was shown in Figure 27. These correspond to mean profiles with the plasma actuator off and on with vane angles of attack of 0, 1, 2, and 3 degrees.

The mean profiles indicate that the plasma actuator located on the suction side of the vane had the effect of increasing the centerline wake velocity, which is indicative of lowering the drag. However it does not appear that the location of the wake centerline was shifted in the spanwise direction that would be indicative of flow vectoring.

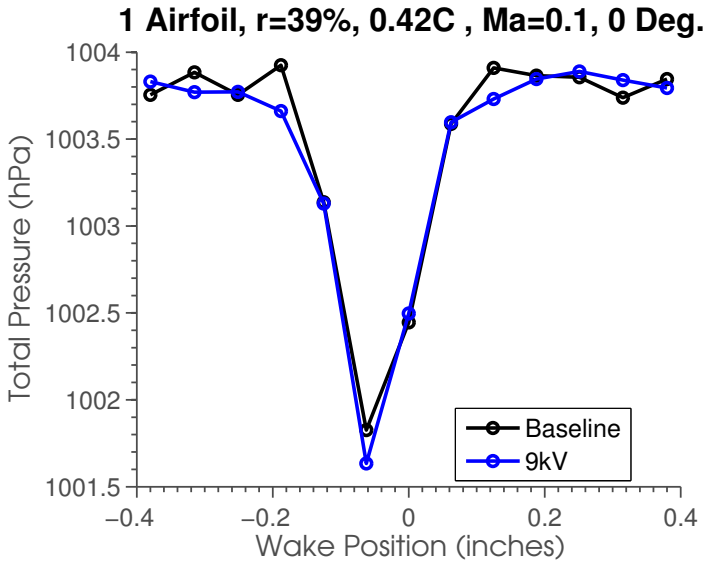

Figure 30: Mean velocity profiles in the wake of the vane with the actuator on the suction-side trailing edge at an angle of attack of 0°.

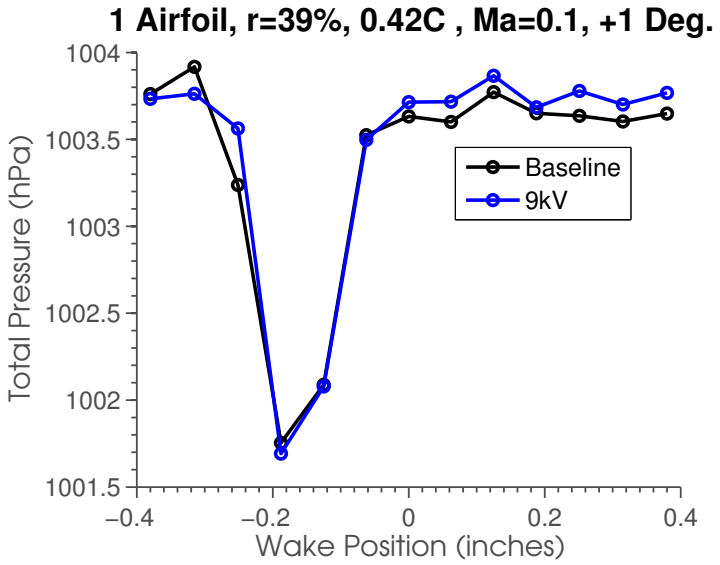

Figure 31: Mean velocity profiles in the wake of the vane with the actuator on the suction-side trailing edge at an angle of attack of 0°.

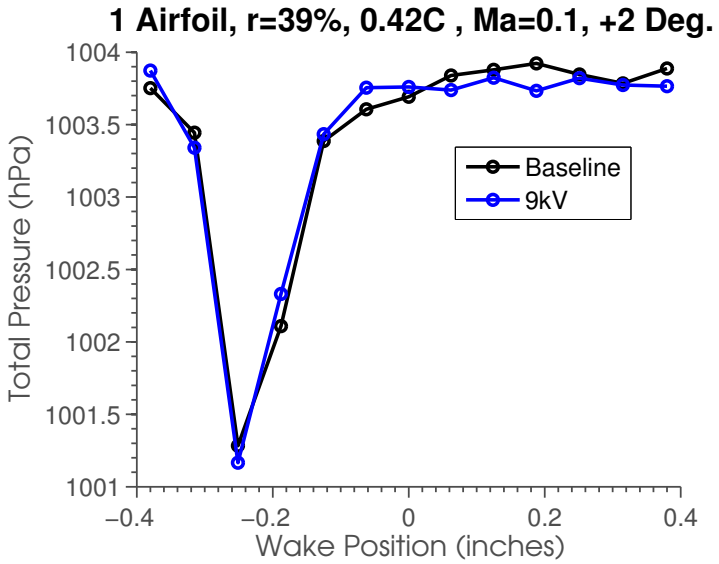

Figure 32: Mean velocity profiles in the wake of the vane with the actuator on the suction-side trailing edge at an angle of attack of 0°.

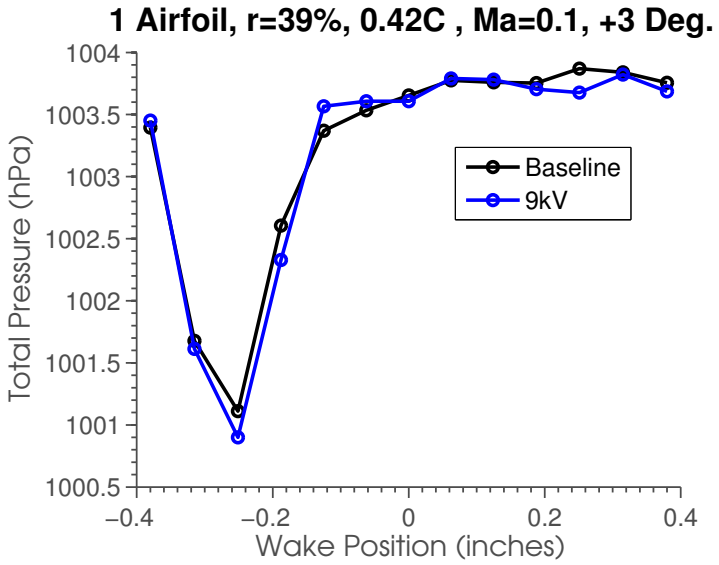

Figure 33: Mean velocity profiles in the wake of the vane with the actuator on the suction-side trailing edge at an angle of attack of 0°.

3.3.2 Pressure-side Actuator

All of the experiments again involved a *single* vane at a free-stream Mach number of 0.1, and with the pulsed-DC voltage amplitude of 9 kV. Mean velocity profiles were measured $0.42c$ downstream of the trailing edge of the vane at a radial location corresponding to 39% of the distance from the center body. Figures 34 to 35 correspond to the cases with the plasma actuator located on the pressure side of the vane as was shown in Figure 28. These correspond to mean profiles with the plasma actuator off and on with vane angles of attack of -2.5 and -5 degrees.

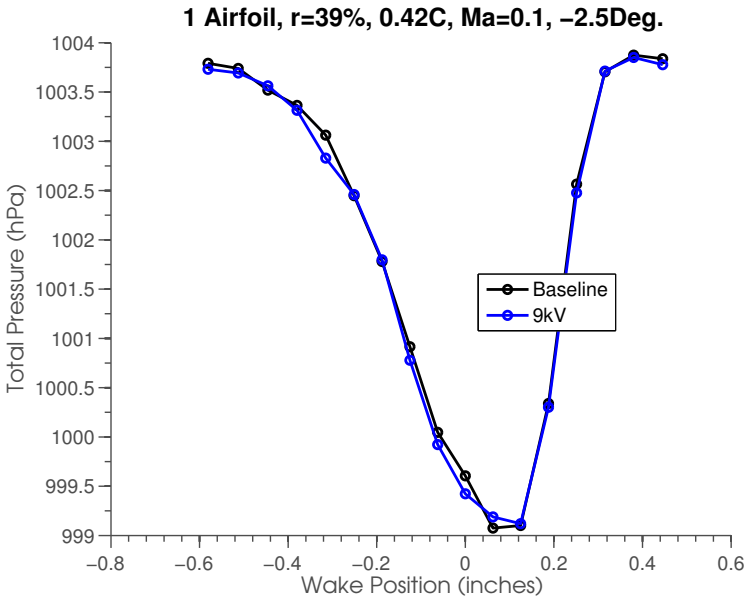

Figure 34: Mean velocity profiles in the wake of the vane with the actuator on the pressure-side trailing edge at an angle of attack of $-2.5°$.

The objective of the pressure-side plasma actuator design was to cause a boundary layer separation bubble near the trailing edge of the vane. To help to achieve this, the vane was oriented at negative angles of attack. We presumed that there would be an optimum negative angle of attack at which the boundary layer near the trailing edge would be on the verge of separating. This angle of attack would then be most receptive to the plasma actuator.

At the smallest negative angle of attack of $-2.5°$ shown in Figure 35, there was a measurable shift of the mean profile with the plasma actuator on, indicative of trailing-edge flow vectoring. This is more apparent with at the $-5°$ angle of attack case shown in Figure 35. Based on examination of other larger negative angles of attack, $-5°$ appeared to be the optimum for this actuator configuration.

In either case with the vane IGV, the effect of the plasma actuator was minimal. The results suggest that the trailing-edge radius is too small to produce the desired effect that was evident on the larger 1/2 in. cylinder. This would suggest that either thicker or truncated vane geometries are needed. Although such designs would increase the pressure loss through the IGV stage, it is possible to reduce this by placing actuators on both sides of the trailing

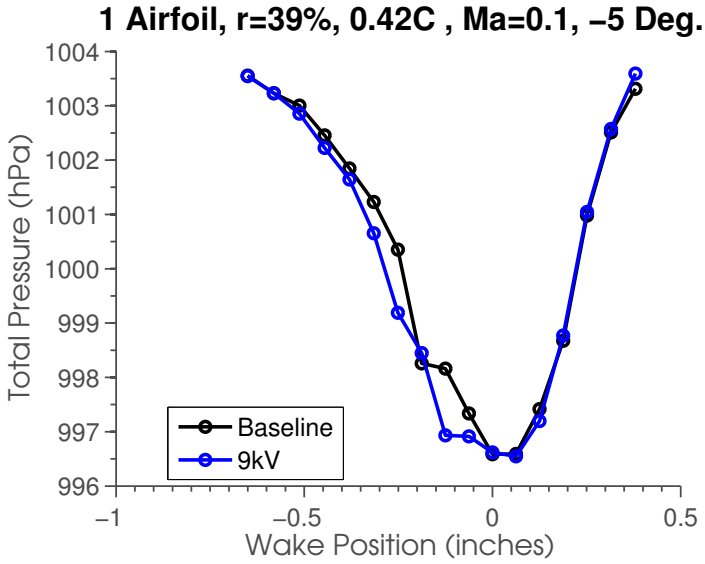

Figure 35: Mean velocity profiles in the wake of the vane with the actuator on the pressure-side trailing edge at an angle of attack of $-5°$.

edge radius. Flow vectoring would then be accomplished by appropriately adjusting the voltage to the two actuators.

4 Summary

The experiments were the first to investigate the uses of the Pulsed-DC plasma actuator for flow separation control, with the objective for vectoring the flow in the wake of bluff bodies. The assumption going in was that the response of the flow would be similar to that of the AC plasma actuator, namely that it would be a quasi-steady effect. Experiments performed in parallel with the present investigation proved this assumption false. In fact the induced velocity field produced by the Pulsed-DC actuator is highly unsteady and therefore merits a different approach that couples the pulsing frequency to the separated shear layer instability frequency to be effective for flow separation control. This was confirmed in flow visualization experiments at the end of this investigation, but was not conceived going in. As a result the operating conditions for the separation control were not optimized.

With that caveat, investigations were performed on an azimuthal array of elements that consisted of circular cylinders of two diameters of 3/16 and 1/2 inches, and an airfoil-shaped IGV vane. In all of these, the location of the plasma actuator relative to the flow separation location is important. This favored the larger cylinder diameter over the smaller cylinder diameter, and the small trailing-edge radius of the IGV vane. In addition, the smaller radii were more sensitive to the small step produced by the exposed electrode and was observed in some cases to passively alter the flow separation. With these factors in mind, the best results were obtained with larger cylinder azimuthal array, producing a 14° flow vector angle change with the Pulsed-DC plasma actuator at Mach 0.1. This result was produced with a pulsing frequency of 500 Hz, which the flow visualization study conducted afterwards indicated was

not optimal. Therefore it is possible that larger flow vector angles are possible in this case. Higher Mach numbers were not investigated. If they had, the optimum pulsing frequerncy would scale linearly with Mach number.

As a general conclusion, it appears that larger trailing-edge radii are preferable for the reasons mentioned. Such shapes will introduce more pressure drag that passively could be objectionable. The solution would be to use plasma actuators on both sides of the trailing edge radius to attach the flow and minimize the wake. The flow vectoring could then be accomplished by adjusting the voltage on one side to favor the other.